Effect of heated wall inclination on natural convection heat transfer in water with near-wall injection of millimeter-sized bubbles

Atsuhide Kitagawa [a,*], Petr Denissenko [b], and Yuichi Murai [c]

[a] Department of Mechanical and System Engineering, Kyoto Institute of Technology, Goshokaido-cho, Matsugasaki, Sakyo-ku, Kyoto 606-8585 Japan

[b] School of Engineering, University of Warwick, Gibbet Hill Road, Coventry CV4 7AL, UK

[c] Laboratory for Flow Control, Faculty of Engineering, Hokkaido University, Kita-13, Nishi-8, Kita-ku, Sapporo 060-8628 Japan

* Corresponding author. Tel: +81 75 724 7327; Fax: +81 75 724 7300; E-mail: kitagawa@kit.ac.jp (A. Kitagawa).

ABSTRACT

Natural convection heat transfer from a heated wall in water with near-wall injection of millimeter-sized bubbles is studied experimentally. Velocity and temperature measurements are conducted in the near-wall region. In the range of the heated wall angles from 0 to 40˚ from the vertical, the heat transfer coefficient increases by up to an order of magnitude with bubble injection. The ratio of the heat transfer coefficient with bubble injection to that without injection increases with the wall inclination angle. Based upon measured liquid temperature distributions and liquid flow velocity profiles, enhancement of heat transfer by bubble injection is explained by two mechanisms. First, wall-parallel transport of cold liquid into the thermal boundary layer is enhanced by the bubble-driven flow. Second, wall-normal mixing of warm liquid and cold liquid occurs, as a result of wall-normal velocity fluctuations of the liquid phase activated by a combination of bubble rising motion, vortex shedding from the bubbles, and unsteady vortices formed within the boundary layer. The unsteady vortices travel along the wall together with the bubbles, primarily contributing to the enhancement of heat transfer at higher wall inclination angles.

Keywords: Bubble injection, Natural convection, Particle tracking velocimetry, Flow visualization

1. Introduction

Natural convection caused by a heated plate [1−4] appears in various types of heat exchangers. With the aim of developing high performance heat exchangers, a number of promising approaches [5−7] have been proposed to enhance natural convection heat transfer. The injection of bubbles is an effective technique, the effect of which on heat transfer depends strongly on the size of injected bubbles. For example, when millimeter-sized bubbles are injected into a convection cell, a significant enhancement of heat transfer is observed along a vertical plate [8−10]. However, as the size of injected bubbles and the gas volumetric flow rate increase, their influence on heat transport tends to decrease because large bubbles move towards the outside of the thin thermal boundary layer because of the wall-repulsive lift [11,12] and bubble-bubble repulsive forces. Smaller bubbles, such as sub-millimeter-sized bubbles and microbubbles [13−15], are relatively easy to inject into the thermal boundary layer [16−18], resulting

in lower energy consumption for bubble injection and, as a consequence, higher efficiency of bubble injection for heat transfer enhancement. Another advantage of small bubbles is their shape-retention force relative to the shear stress induced inside the boundary layer, i.e., bubbles at small capillary numbers. This feature provides effective mixing of the liquid beyond the thermal boundary layer, enhancing gross heat transfer. Nevertheless, we cannot use even smaller bubbles to enhance heat transfer because a different phenomenon involving wettability takes place in the proximity of the wall. As we reported in a previous paper [19], we found that small bubbles, especially microbubbles, readily adhere to a vertical wall with poor wettability (Fig. 1). This forms a thermal insulation layer between the wall and the liquid, resulting in heat transfer deterioration [20]. Even when there is good wettability, bubble-wall attachment tends to occur when the wall angle deviates from the vertical. Summarizing the above, the optimal bubble size should be intermediate, i.e., such bubbles are not separated from the heated wall and do not form a thermal insulation layer along the wall. We therefore conclude that it is important to study the effect of millimeter-sized bubbles on heat transfer enhancement, which is dependent on the inclination angle of the heated wall. Compared with smaller bubbles, millimeter-sized bubbles are not affected by wall wettability or other electro-chemical properties of the solid wall surface at the molecular scale, so that a certain thermo-fluid similarity is expected to be found, regardless of the material constituting the wall or chemical modification of the wall surface. In the case of forced convection, which is not the subject of this paper, the effects of millimeter-sized bubbles or microbubbles on heat transfer can be found in Refs. [21−24].

The following three studies on the influence of millimeter-sized bubbles on natural convection heat transfer from an inclined heated plate are particularly relevant to the current work. Qiu and Dhir [25] carried out velocity and temperature measurements in the liquid around a single vapor bubble and a series of vapor bubbles sliding along a downward-facing inclined heater surface. They introduced particle image velocimetry (PIV) and holographic interferometry to the target volume, and quantitatively visualized the heat transfer enhancement events that were formation and shedding of vortices behind the bubble. Bayazit et al. [26] investigated natural convection heat transfer from a heated surface in FC-87 coolant into which a single, wall-sliding, deformable vapor bubble was injected. When they set the angle of the heated surface at 12˚ from the horizontal, they found that not only the bubble's wake but also the micro-layer surrounding the bubble contributed to the local heat transfer rate. Delaure et al. [27] investigated the interaction of a single, rising, ellipsoidal air bubble with natural convection from an inclined heated flat surface in water. They used PIV, thermocouples, and a hot film sensor to prove that the zigzagging motion of the bubble affects the local temperature and heat flux at the surface. From these three studies, we can understand that the inclination angle of the heated wall has a strong impact on the thermal boundary layer thickness, the bubble shape [28], the bubble upward motion, and the wake structure behind the bubble [29,30]. In addition, when bubbles are intensively injected near the inclined heated wall, we must consider the effect of upward liquid flow. Because bubble-driven upward flow affects bubble number density and size distributions, i.e., onset of a two-way interaction between the gas and liquid phases, it is possible that flow plays a significant role in heat transfer over a wide range of wall inclination angle.

The purpose of this study is to experimentally clarify the effect of the inclination angle of a heated plate on non-boiling natural convection heat transfer in water with injection of millimeter-sized bubbles. This work is expected to provide insights into phenomenological continuity from the case of a vertical wall to the inclined geometry. In our experiments, bubbles are intensively injected close to the heated plate so that a bubble-induced velocity boundary layer is formed in addition to the thermal boundary layer along the heated wall. Hence, not only the quasi-static thermal properties, but also two-way interacting dynamics in heat transfer are the targets of our exploration. To this end, the particle tracking velocimetry (PTV) technique and micro-thermocouples are used for velocity and temperature measurements, respectively. Finally, we discuss in detail the mechanism behind changes in heat transfer by bubble injection.

2. Experimental setup

A schematic of the experimental apparatus is given in Fig. 2. The apparatus consists of a transparent acrylic tank (2000 mm high, 200 mm wide, and 150 mm deep), a heated plate, a DC power supply (Takasago, ZX−400L), a bubble generator, a peristaltic pump (Azone, DSP−100SA), a water-cooled heat exchanger, and a low-temperature thermostatic bath (Azone, LTB−250). The heated plate is aligned parallel to the inside wall of the tank, and the bubble generator is located below the tank. The *x*, *y*, and *z* axes are defined along the streamwise, wall-normal and spanwise directions, and *x*, *y*, and *z* are, respectively, zero at the starting point of the heated section, at the surface of the heated plate, and at the center of the plate. The inclination angle of the heated plate, ϕ, is defined as the angle between the *x* axis and the vertical direction, and is set by directly inclining the tank such that the heated surface faces downward. The liquid temperature at a location sufficiently far from the heated plate is controlled using the water-cooled heat exchanger installed in the upper part of the tank and the low-temperature thermostatic bath.

A schematic of the heated plate is given in Fig. 3. To heat the surface of the acrylic plate, providing a constant wall heat flux, 20-μm-thick strips of stainless-steel foils are attached to its surface at 0.5 mm intervals. Taking into account the accuracy and reliability of temperature measurements with and without bubble injection, the wall heat flux is set to 1480 W/m^2. The heated section ranges from 0 to 825 mm, and the starting point of the section is 100 mm above the bubble injection position (i.e., the bottom of the tank). The plate is entirely covered by 25-μm-thick Kapton tape to prevent electrical leakage. In addition, a 5-mm-thick air layer is placed inside the plate to suppress heat leakage behind the plate. The heat loss through the back of the heated plate is estimated to be less than 3% of the total wall heat flux.

A schematic of the bubble generator is given in Fig. 4. Air bubbles are injected through five needles (0.36 mm inner diameter and 0.5 mm outer diameter) into a test section using the peristaltic pump. The needles are located at x=−100 mm, y=10 mm, and z=−50, −25, 0, 25, 50 mm. The bubble flow rate is set to 100 ml/min to suppress the occurrence of bubble coalescence. In this case, the bubble injection frequency is estimated at 25 Hz. According to our analysis through image processing, the mean bubble diameter, calculated from the circle-equivalent value for the area of each bubble image, ranges from 2.3 to 2.8 mm.

The experimental procedure in our experiments is as follows: (1) The container is filled with water at 22 ˚C to 50 mm from the top of the tank. (2) After the water is thoroughly mixed, it is left for 10 min to reduce liquid disturbance. (3) The heating system is run for 10 min to stabilize the heated plate sufficiently before temperature and velocity measurements begin.

3. Measurement techniques

3.1. Temperature measurement

The temperature measurement system consists of K-type 100-μm-thermocouples, a reference junction, a data acquisition unit, and a personal computer. To measure the surface temperature of the heated plate T_W, 24 micro-thermocouples are attached to the stainless-steel foils through 1.5-mm-diameter holes on the back of the heated plate. The holes are completely filled with silicone sealant to prevent water from flowing into them. The position of each thermocouple is given in Table 1. In addition, a single micro-thermocouple is set at x=370 mm, y=175 mm and z=0 mm, to measure the liquid temperature at a location sufficiently far from the plate, $T_{L\infty}$. The micro-thermocouples are accurate to within ±0.125 ˚C. The sampling frequency is set at 5 Hz. Data acquisition is carried out for 540 s after the bubble injection begins, and the data is averaged from 510 to 540 s. The local heat transfer

coefficient is estimated using Eq. (1).

$$h_x = \frac{q_W}{T_W - T_{L\infty}}, \tag{1}$$

where q_W is the wall heat flux. The local liquid temperature, T_L, near the heated wall, is measured using a single micro-thermocouple (Fig. 3). This thermocouple is traversed with an accuracy of ±0.06 mm in the *y* direction using an *x*–*y* stage installed at the top of the tank. The effect of the presence of the traversing micro-thermocouple on natural convection heat transfer is negligible (Appendix A.1).

3.2. Two-phase velocity measurement

In this study, the PTV and shadow image techniques are used for two-phase velocity measurements. A schematic of the velocity measurement system is given in Fig. 5. This system consists of a color charge-coupled device (CCD) camera (IMPERX, ICL−B0620C−KC000) with a resolution of 640×480 pixels, a diode-pumped solid-state (DPSS) laser (Laser QUANTUM, excel mpc 6000), cylindrical lenses, a neutral density (ND) filter, a red light-emitting diode (LED) source (CCS, TH−63X60RD), and a personal computer. Two-phase images are taken with the color CCD camera. Porous particles of diameter and specific gravity 60 μm and 1.02, respectively, are used as tracer particles. The particle concentration is set at 60 ppm, so that the effect of particles on the two-phase flow field can be neglected. Particles are illuminated by a 2-mm-thick laser sheet, produced by the cylindrical lenses. In contrast, bubbles are illuminated using the red LED source to capture bubble images as shadow images. The measurements are taken in the *x*−*y* plane. The experimental conditions for the velocity measurements are given in Table 2.

In the image processing, RGB components of the color images taken with the color CCD camera are used to obtain the two-phase velocities. Green and red images are used to measure the liquid and bubble velocities, respectively. Only bubbles in the plane of the laser sheet are used for the bubble velocity measurement. The image processing procedure is described in detail in Ref. [31]. In the case of bubble injection, the uncertainty in the liquid velocity associated with particle centroid detection is estimated to be 3.0 mm/s, which corresponds to approximately 4.2% of the maximum value of the wall-parallel mean velocity of the liquid phase (71.2 mm/s). The uncertainty in bubble velocity associated with bubble centroid detection is estimated to be 1.8 mm/s, which corresponds to approximately 0.5% of the maximum value of the wall-parallel mean velocity of bubbles (338.8 mm/s). To obtain reliable data, 6,000 images are used under each experimental condition.

4. Results and discussion

4.1. Single-phase natural convection

Fig. 6 shows the relationship between the modified Rayleigh number, $Ra_{x\phi}^{*}$, and the local Nusselt number, Nu_x, for single-phase natural convection [32−35], defined as follows:

$$Ra_{x\phi}^{*} = \frac{\beta q_W x^4 g \cos\phi}{k\nu\alpha}, \tag{2}$$

$$Nu_x = \frac{h_x x}{k}, \tag{3}$$

where β is the volumetric thermal expansion coefficient, g is the gravitational acceleration, k is the thermal

conductivity, ν is the kinematic viscosity, and α is the thermal diffusivity. For comparison, the following empirical equations for laminar and turbulent natural convection are used [36].

(Laminar natural convection) $$Nu_x = C_1 \cdot \left(Ra^*_{x\phi}\right)^{0.2}, \tag{4}$$

(Turbulent natural convection) $$Nu_x = C_2 \cdot \left(Ra^*_{x\phi}\right)^{0.22}, \tag{5}$$

where the constant values in these equations are defined as C_1=0.6 and C_2=0.568, based on the paper of Vliet and Liu [37]. In the range $1.0\times10^9<Ra_{x\phi}^*<2.4\times10^{12}$, there is less than a 5% difference between each experimental result at ϕ=0˚ and the solid line representing Eq. (4). This means that laminar flows exist in the range $1.0\times10^9<Ra_{x\phi}^*<2.4\times10^{12}$ (i.e., 0<x<470 mm) while transition from laminar flow takes place in the range $2.4\times10^{12}<Ra_{x\phi}^*<1.6\times10^{13}$ (i.e., 470<x<770 mm). In the case of ϕ=20 and 40˚, in contrast, there is less than a 5% difference between each experimental result and the solid line representing Eq. (4), and therefore, at both values of ϕ, laminar flow exits over the heated section.

4.2. Local temperature in liquid phase

The distributions of the liquid temperature difference, T_L–$T_{L\infty}$, are shown in Fig. 7. In this figure, ″TPF″ and ″SPF″ represent two-phase and single-phase flows, respectively. Results for the 2-D simulation of single-phase natural convection, performed by our group [38], are also shown in Fig. 7. Considering the notable change in thermal boundary layer thickness caused by near-wall injection of bubbles, this study defines two types of thicknesses. One is the thickness of the effective thermal boundary layer, δ_{TE}, and is estimated using Eq. (6).

$$\delta_{TE} \approx \frac{k\left(T_W - T_{L\infty}\right)}{q_W}. \tag{6}$$

The other is the thickness of the actual thermal boundary layer, δ_T, and is estimated as the distance from the heated wall to the y location where T_L–$T_{L\infty}$=0.05 ˚C (i.e., the minimum value of the vertical axis) using exponential fits to experimental data in Fig. 7. Table 3 lists δ_{TE} and δ_T for the cases with and without bubble injection at each wall inclination angle, estimated from Fig. 7. At all values of ϕ, bubble injection leads to a significant decrease in the liquid temperature close to the heated wall, as shown in Fig. 7. Moreover, at all values of ϕ, δ_{TE} becomes very short, while δ_T becomes quite long, as a result of bubble injection (Table 3). In particular, the case at ϕ=40˚ exhibits a notable change in these thicknesses.

4.3. Heat transfer coefficient and efficiency of bubble injection

The relationship between the measurement position, x, and the heat transfer coefficient, h_x, is shown in Fig. 8. At all values of ϕ, h_x is significantly higher under bubble injection than without injection over the heated section. The ratio of h_x with bubble injection to that without injection (hereafter called ″heat transfer coefficient ratio″) ranges from 2.4 to 5.5. In addition, in the case of bubble injection, h_x increases with increasing ϕ. However, the rate of increase in h_x decreases as ϕ increases. This implies that there would exist an optimal ϕ for enhancing natural convection heat transfer. Similar trends were also seen at a bubble flow rate of 50 ml/min (Appendix B.1).

Fig. 9 shows the relationship between the inclination angle of the heated plate and the efficiency of bubble injection, η. Given the constant wall heat flux condition used in this study, and from the general definition of the coefficient of performance (COP), η is defined based on the heat transfer coefficient ratio as follows:

$$\eta = \frac{q_W A_H}{P}\left[\left(\frac{\overline{h_{x\_TPF}}}{h_{x\_SPF}}\right)-1\right], \tag{7}$$

where A_H is the total area of the heated section, and P is the power required for the bubble injection. A high accuracy power meter (NTT−AT, SHW3A) was used to measure the power consumption of the peristaltic pump. At all values of ϕ, η is higher than 13. In particular, at ϕ=40˚, η reaches up to approximately 27. In addition, η increases with increasing ϕ and this trend does not change qualitatively even if another pump is used. It is concluded from Figs. 8 and 9 that in the range $0 \le \phi \le 40$˚, the injection of bubbles is a highly effective and efficient technique for enhancing natural convection heat transfer in water and that its effectiveness and efficiency increase with ϕ.

In the following, we discuss in detail the change in heat transfer mechanism caused by bubble injection using mainly two-phase velocity measurements at x=170 mm, which corresponds to the laminar region in single-phase natural convection.

4.4. Bubble concentration and wall-parallel mean velocity of bubbles

The profiles of the bubble concentration in the wall-normal direction, ε, are shown in Fig. 10. ε is estimated as the ratio of the local bubble to liquid projection areas in each red image. The vertical axis is normalized by ε_{sum} which is the sum of ε. Bubbles are located in the range $0<y<20$ mm at ϕ=0˚, $0<y<8$ mm at ϕ=20˚, and $0<y<4$ mm at ϕ=40˚. In other words, the accumulation of bubbles near the heated wall becomes more notable as ϕ increases. As expected, the wall-normal component of buoyancy acting on bubbles, which forces them to move towards the wall, increases with increasing ϕ. Consequently, the diffusion of bubbles in the wall-normal direction is suppressed at higher ϕ. Moreover, according to our visualization in the x−y and x−z planes, both the bubble-wall attachment as seen for smaller bubbles (Fig. 1) and the bubble cluster as seen in a vertical channel bubbly flow [39] do not occur at any ϕ, even though rising bubbles are located close to the wall, especially at ϕ=40˚. We speculate that the former relates to the buoyancy/surface tension ratio of injected bubbles, while the latter relates mainly to their interface shape and local bubble number density.

The profiles of the mean velocity of bubbles in the wall-parallel direction, u_G, are shown in Fig. 11. It is clear from this figure that at all values of ϕ, u_G is above 200 mm/s. Considering that the maximum value of the wall-parallel mean velocity of the liquid phase for single-phase natural convection is approximately 10 mm/s at each wall inclination angle (Fig. 12), even near the wall, bubbles rise at a speed of at least 20 times higher than single-phase natural convection. This means that each injected bubble has the potential to entrain surrounding liquid. It is also clear from this figure that the case at ϕ=20˚ exhibits the highest u_G near the wall. This trend differs from the bubble concentration distribution. As shown in Fig. 10, the bubble concentration near the wall increases with increasing ϕ. Usually, an increase in bubble concentration leads to an increase in the local buoyancy source, which can induce an upward liquid flow at high speed, and as a result, u_G tends to increase. However, when bubbles rise along the inclined wall, the wall-parallel component of buoyancy acting on them decreases with increasing ϕ. In the case of ϕ=40˚, the geometric factor becomes dominant. Considering that the wall-parallel velocity of a single bubble near the wall decreases monotonically with increasing ϕ [40], the non-monotonous dependence of the wall-parallel mean velocity of bubbles on the wall inclination is recognized as a unique feature observed in the case of near-wall injection of bubbles.

4.5. Wall-parallel mean velocity and root-mean-square of wall-normal fluctuation velocity of liquid phase

The profiles of the mean velocity of liquid phase in the wall-parallel direction, u_L, are shown in Fig. 12. At all

values of ϕ, u_L is significantly increased by bubble injection over a wide range of y. In particular, the ratio of the maximum u_L with bubble injection to that without injection is 5.3 at ϕ=0˚, 6.4 at ϕ=20˚, and 6.4 at ϕ=40˚. This arises from liquid entrainment by rising bubbles, because under our experimental conditions, bubbles rise near the wall at much higher velocity than under single-phase natural convection, as mentioned in Fig. 11. Usually, an increase in wall-parallel liquid velocity near the heated wall enhances transport of cold liquid from the unheated section into the thermal boundary layer, hence causing heat transfer enhancement. In addition, in the case of bubble injection, in the vicinity of the heated wall (0<y<4 mm), the case at ϕ=20˚ exhibits the highest u_L.

The profiles of the root-mean-square (RMS) of the fluctuation velocity of the liquid phase in the wall-normal direction, $<v'_L v'_L>^{0.5}$, are shown in Fig. 13. The vertical axis is normalized by the maximum value of the mean velocity of the liquid phase in the wall-parallel direction without bubble injection, u_{Lm}, at each wall inclination angle. At all values of ϕ, $<v'_L v'_L>^{0.5}/u_{Lm}$ is markedly increased by the injection of bubbles over a wide range of y. As is well-known, an increase in the RMS of wall-normal liquid fluctuation velocity near a heated wall enhances mixing of warm liquid close to the heated wall and cold liquid at the edge of the thermal boundary layer, enhancing heat transfer. In addition, in the case of bubble injection, near the heated wall (0<y<4 mm), $<v'_L v'_L>^{0.5}/u_{Lm}$ increases with increasing ϕ.

To evaluate the influence of bubble injection on heat transfer, we consider the ratio of the actual thermal boundary layer thickness, δ_T, to the velocity boundary layer thickness, δ_V, the wall-parallel velocity of liquid phase averaged over the thermal boundary layer thickness, $u_{L\delta}$, and the eddy diffusivity in the boundary layer, K_{eddy}. Table 4 lists δ_T/δ_V for the cases with and without bubble injection at each wall inclination angle. Here, δ_V is defined as the distance from the heated wall to the y location where u_L is equal to zero, and is estimated from Fig. 12. It is clear from Table 4 that at ϕ=20 and 40˚, δ_T/δ_V for the case with bubble injection tends to approach 1.0, compared with that for the case without injection. This means that the interaction between the velocity and temperature fields becomes stronger because of bubble injection. This trend can be more clearly seen at ϕ=40˚ than at ϕ=20˚. Table 5 lists $u_{L\delta}$ and K_{eddy} at each wall inclination angle. K_{eddy} is given by

$$K_{eddy} \approx l_e \cdot \left\langle v'_L v'_L \right\rangle^{0.5}, \tag{8}$$

where l_e is the typical eddy size. In Table 5, the thickness of the effective thermal boundary layer (i.e., δ_{TE}) for the case without bubble injection is used to simplify calculations. Based on this, we assume that $l_e=\delta_{TE}$. The value of $<v'_L v'_L>^{0.5}$ in Eq. (8) is calculated from Fig. 13 as the RMS of the wall-normal fluctuation velocity of the liquid phase averaged over δ_{TE}. It is clear from Table 5 that at all values of ϕ, $u_{L\delta}$ increases more than four times in the bubble-driven flow and K_{eddy} is one or two orders of magnitude higher than the molecular thermal diffusivity. Note that this trend becomes more significant if the thickness of the actual thermal boundary layer (i.e., δ_T) is used instead of δ_{TE}. The estimation indicates that the bubble-driven wall-parallel flow significantly enhances the wall-parallel transport of cold liquid from the unheated section into the effective thermal boundary layer, while the eddy diffusivity created by bubble injection facilitates the wall-normal mixing of warm and cold liquids in the boundary layer. Therefore, both effects make a major contribution to the heat transfer enhancement shown in Fig. 8. In particular, they result in the thinning of the effective thermal boundary layer, especially at ϕ=40˚ when bubbles accumulate close to the heated wall.

4.6. Bubble behavior near heated wall

To understand the bubble behavior near the heated wall, typical time-series images of bubbles near the heated wall are shown in Fig. 14, and the bubble Reynolds number, Re_G, and the RMS of the bubble fluctuation velocity

in the wall-normal direction, $\langle v'_G v'_G \rangle^{0.5}$, are shown in Fig. 15 as a function of ϕ. Similar to Fig. 13, the right-hand vertical axis is normalized by u_{Lm} at each wall inclination angle. Re_G is based on the slip velocity between the bubble and the surrounding liquid. We can observe wobbling, bouncing, and sliding motions [40−42], exhibited by encircled bubbles in Fig. 14. These motion patterns strongly depend upon ϕ. It is clear from Fig. 15 that at all values of ϕ, Re_G is higher than 550. Considering other researchers' findings that vortex shedding from the bubble interface can be observed at $Re_G \geq 410$ [30], it is quite possible that at all values of ϕ, vortex shedding from bubbles occurs even though most of bubbles accumulate close to the heated wall, especially at ϕ=40˚. As expected, the bubble rising motions and vortices shed from bubble interface contribute to the liquid mixing. However, it is also clear from Fig. 15 that $\langle v'_G v'_G \rangle^{0.5}/u_{Lm}$ increases with decreasing ϕ, indicating that bubble motion is less stationary and the intensity of shed vortices (i.e., liquid velocity fluctuations) is higher at lower ϕ. Thus, the randomness of wall-normal bubble motion does not correlate with the RMS of the wall-normal fluctuation velocity of the liquid phase near the heated wall (Fig. 13). For this reason, there would exist an additional factor that induces liquid mixing near the heated wall, apart from the bubble rising motion and the vortex shedding from the bubbles.

4.7. Correlation between wall-parallel and wall-normal fluctuation velocities of liquid phase

To further investigate the liquid mixing mentioned in Section 4.6, scatter plots of the liquid fluctuation velocities near the heated wall are shown in Fig. 16. In this figure, u'_L is the fluctuation velocity of the liquid phase in the wall-parallel direction, and the horizontal and vertical axes are normalized by u_{Lm} at each wall inclination angle. cc is the correlation coefficient between u'_L and v'_L, defined as follows:

$$cc = \frac{\langle u'_L v'_L \rangle}{\langle u'_L u'_L \rangle^{0.5} \cdot \langle v'_L v'_L \rangle^{0.5}}. \tag{9}$$

In addition, the time evolution of the distance between the location of the peak in the Reynolds shear stress profile and the heated wall, y_R, for the case with bubble injection is shown in Fig. 17. The Reynolds shear stress is defined as $\langle u'_L v'_L \rangle$. Each y_R is averaged over a period of 5 s. At ϕ=0˚, the distribution of u'_L/u_{Lm} and v'_L/u_{Lm} is expanded by the injection of bubbles, but its distribution remains almost isotropic (Fig. 16). In contrast, at ϕ=20 and 40˚, a significant expansion of the distribution caused by bubble injection can be seen in the first and third quadrants, and there is a positive correlation between u'_L and v'_L. In particular, the positive correlation between them is more remarkable at ϕ=40˚ than at ϕ=20˚. Moreover, y_R at all values of ϕ changes with time, and y_R becomes shorter at higher ϕ (Fig. 17). The results obtained from Figs. 16 and 17 imply that in the case of bubble injection, there exist unsteady vortices with their major axes in the spanwise direction of the flow field, similar to the vortices observed in a turbulent natural convection boundary layer [43], and they tend to approach the heated wall at higher ϕ. In Section 4.8, we describe such vortices induced by bubble injection using flow visualization.

4.8. Flow visualization and relationship between normalized liquid temperature reduction and normalized Reynolds shear stress

Figs. 18 and 19 show flow visualization using fluorescent dye and the relationship between the normalized reduction in liquid temperature by bubble injection, λ_T, and the normalized Reynolds shear stress, λ_R, respectively. In Fig. 19, λ_T and λ_R are given by

$$\lambda_T = \frac{T_{L\_SPF} - T_{L\_TPF}}{\left| T_{W\_SPF} - T_{W\_TPF} \right|}, \tag{10}$$

$$\lambda_R = \frac{\langle u'_L v'_L \rangle}{\langle u'_L v'_L \rangle_m}, \tag{11}$$

where $<u'_L v'_L>_m$ is the maximum of the Reynolds shear stress at each wall inclination angle. In Fig. 19, y is the distance from the heated wall. In the case of bubble injection, at all values of ϕ, the vortex can be clearly seen in the flow field (Fig. 18). Moreover, the generated vortices are significantly larger than the individual bubbles, and each vortex has a clockwise rotation. Considering the above and that y_R is consistently within the negative gradient region in the profile of the wall-parallel mean velocity of the liquid phase (Figs. 12 and 17), we expect that the relatively large unsteady vortices in the flow field are not shed from the bubble interface but occurred from instability of the bubble-driven upward flow. With increasing ϕ, the unsteady vortices tend to approach closer to the heated wall (Figs. 17 and 18), and as a consequence, the correlation between λ_T and λ_R becomes stronger (Fig. 19). This implies that at ϕ=40˚, the unsteady vortex makes a significant contribution to the most active mixing of warm and cold liquids. Because of the heat exchange resulting from this active mixing, both the decrease in the liquid temperature close to the heated wall and the expansion of the thermal boundary layer become more significant at ϕ=40˚ than at ϕ=0 and 20˚, as shown in Fig. 7. Note that under our experimental conditions, the increase in the correlation between u'_L and v'_L (as seen in Fig. 16) is not affected by transition to turbulence in the natural convection boundary layer caused by bubble injection. This is because a similar trend was also observed under non-heating conditions.

From the above results, the mechanism of heat transfer enhancement by the near-wall injection of millimeter-sized bubbles is summarized as follows (Fig. 20): In the case of bubble injection, in the range $0 \le \phi \le 40$˚, enhancement of natural convection heat transfer from the heated plate arises from both the active transport of cold liquid from the unheated section into the thermal boundary layer and the wall-normal mixing of warm liquid and cold liquid. The former arises because of the bubble-driven flow in the wall-parallel direction, while the latter is due to the wall-normal velocity fluctuations of the liquid phase, activated by a combination of the bubble rising motion, the vortex shedding from the bubbles, and unsteady vortices. In particular, unsteady vortices which can markedly intensify the wall-normal mixing, exist closer to the heated wall at higher ϕ. As a result, both the heat transfer coefficient and the efficiency of bubble injection increase with ϕ.

5. Conclusions

In this study, we have investigated the effect of inclination angle of a heated plate, ϕ, on the natural convection heat transfer in water with millimeter-sized bubbles. Velocity and temperature measurements as well as flow visualizations have been performed to study the structure of the near-wall boundary layer under a constant wall heat flux. In the range $0 \le \phi \le 40$˚, the ratio of the heat transfer coefficient with bubble injection to that without injection (heat transfer coefficient ratio) ranges from 2.4 to 5.5 and the efficiency of bubble injection varies from 13 to 27. In addition, both the heat transfer coefficient ratio and the efficiency of bubble injection increase with increasing ϕ. In other words, in the range $0 \le \phi \le 40$˚, the injection of millimeter-sized bubbles is a highly effective and efficient technique for enhancing natural convection heat transfer in water, and its effectiveness and efficiency increase with ϕ. The enhancement of natural convection heat transfer with bubble injection is explained by two mechanisms. One is the active transport of cold liquid from the unheated section into the thermal boundary layer, which is caused by the bubble-driven flow in the wall-parallel direction. The other is the mixing of warm liquid close to the heated wall and cold liquid at the edge of the thermal boundary layer, which results from the wall-normal velocity fluctuations of liquid phase activated by a combination of the bubble rising motion, the vortex shedding from the bubbles, and unsteady vortices. Both the active transport of cold liquid in the wall-parallel

direction and the mixing of warm liquid and cold liquid in the wall-normal direction result in the thinning of the effective thermal boundary layer and a significant decrease in the wall temperature at a fixed wall heat flux. The unsteady vortices induced by the instability of the bubble-driven wall-parallel flow at higher speeds exist near the heated wall at higher ϕ, primarily contributing to a significant increase in both the heat transfer coefficient ratio and the efficiency of bubble injection.

Nomenclature

A_H	total area of heated section [m^2]
cc	correlation coefficient between wall-parallel and wall-normal fluctuation velocities of liquid phase [−]
g	gravitational acceleration [m/s^2]
h_x	heat transfer coefficient [W/m^2K]
k	thermal conductivity [W/mK]
K_{eddy}	eddy diffusivity [m^2/s]
l_e	typical eddy size [mm]
Nu_x	local Nusselt number [−]
P	power required for bubble injection [W]
q_w	wall heat flux [W/m^2]
$Ra_{x\phi}^*$	modified Rayleigh number [−]
Re_G	bubble Reynolds number [−]
T_L	local liquid temperature [˚C]
T_W	surface temperature of heated plate [˚C]
T_∞	liquid temperature far from heated plate [˚C]
u_G	wall-parallel mean velocity of bubbles [mm/s]
u_L	wall-parallel mean velocity of liquid phase [mm/s]
u'_L	wall-parallel fluctuation velocity of liquid phase [mm/s]
v'_G	wall-normal fluctuation velocity of bubbles [mm/s]
v'_L	wall-normal fluctuation velocity of liquid phase [mm/s]
y_R	distance between location of peak in Reynolds stress profile and heated wall [mm]

Greek symbols

α	thermal diffusivity [m^2/s]
β	volumetric thermal expansion coefficient [1/K]
δ_T	thickness of actual thermal boundary layer [mm]
δ_{TE}	thickness of effective thermal boundary layer [mm]
δ_V	thickness of velocity boundary layer [mm]
ε	bubble concentration in wall-normal direction [−]
ε_{sum}	sum of ε [−]
η	efficiency of bubble injection [−]
λ_R	normalized Reynolds shear stress [−]
λ_T	decreasing rate of liquid temperature by bubble injection [−]
ν	kinematic viscosity [m^2/s]
ϕ	inclination angle of heated plate [˚]

Acknowledgements

The authors gratefully acknowledge support from a Grant-in-Aid for Scientific Research (C) (Grant no. 25420160) and a research grant from Kansai Research Foundation for Technology Promotion. In addition, the authors wish to thank Mr. Y. Kimura, Mr. S. Kumokawa and Mr. Y. Nagai of Kyoto Institute of Technology for their assistance with data collection.

Appendix A. Effect of existence of a traversing micro-thermocouple on heat transfer

Fig. A.1 shows a comparison between the heat transfer coefficients with and without a traversing micro-thermocouple. Γ is the ratio of the heat transfer coefficient with the traversing micro-thermocouple to that without the thermocouple. Fig. A.1 clearly shows that in all cases, Γ is approximately 1.0.

Appendix B. Heat transfer coefficient at a bubble flow rate of 50 ml/min

Fig. B.1 shows the relationship between the measurement position x and the heat transfer coefficient h_x at a bubble flow rate of 50 ml/min.

References

[1] K.E. Hassan, S.A. Mohamed, Natural convection from isothermal flat surfaces, Int. J. Heat Mass Transfer 13 (1970) 1873–1886.
[2] T.S. Chen, H.C. Tien, B.F. Armaly, Natural convection on horizontal, inclined, and vertical plates with variable surface temperature or heat flux, Int. J. Heat Mass Transfer 29 (1986) 1465–1478.
[3] T. Inagaki, K. Komori, Heat transfer and fluid flow of natural convection along a vertical flat plate in the transition region: experimental analysis of the wall temperature field, Int. J. Heat Mass Transfer 38 (1995) 3485–3495.
[4] M.Z. Abedin, T. Tsuji, Y. Hattori, Direct numerical simulation for a time-developing natural-convection boundary layer along a vertical flat plate, Int. J. Heat Fluid Flow 52 (2009) 4525–4534.
[5] T. Inagaki, K. Komori, Heat transfer of natural convection along a vertical flat plate using various projections-heat transfer and wall temperature pattern, Trans. JSME (Ser. B) 57 (1991) 3873–3878. (in Japanese)
[6] T. Misumi, K. Kitamura, Heat transfer enhancement of natural convection and development of a high-performance heat transfer plate, JSME Int. J. Ser. B: Fluids Therm. Eng. 36 (1993) 143–149.
[7] T. Tsuji, T. Kajitani, T. Nishino, Heat transfer enhancement in a turbulent natural convection boundary layer along a vertical flat plate, Int. J. Heat Fluid Flow 28 (2007) 1472–1483.
[8] M. Tamari, K. Nishikawa, The stirring effect of bubbles upon the heat transfer to liquids, Heat Transfer-Japanese Research 5 (1976) 31–44.
[9] A.T. Tokuhiro, P.S. Lykoudis, Natural convection heat transfer from a vertical plate-I. Enhancement with gas injection, Int. J. Heat Mass Transfer 37 (1994) 997–1003.
[10] A.T. Tokuhiro, P.S. Lykoudis, Natural convection heat transfer from a vertical plate-II. With gas injection and transverse magnetic field, Int. J. Heat Mass Transfer 37 (1994) 1005–1012.
[11] R. Adoua, D. Legendre, J. Magnaudet, Reversal of the lift force on an oblate bubble in a weakly viscous linear shear flow, J. Fluid Mech. 628 (2009), 23–41.
[12] K. Sugiyama, F. Takemura, On the lateral migration of a slightly deformed bubble rising near a vertical plane

wall, J. Fluid Mech. 662 (2010) 209–231.
[13] B.D. Johnson, R.C. Cooke, Generation of stabilized microbubbles in seawater, Science 213 (1981) 209–211.
[14] E. Dressaire, R. Bee, D.C. Bell, A. Lips, H.A. Stone, Interfacial polygonal nanopatterning of stable microbubbles, Science 320 (2008) 1198–1201.
[15] Y. Murai, Frictional drag reduction by bubble injection (review), Exp. Fluids 55 (2014) 1773–1800.
[16] A. Kitagawa, K. Kosuge, K. Uchida, Y. Hagiwara, Heat transfer enhancement for laminar natural convection along a vertical plate due to sub-millimeter-bubble injection, Exp. Fluids 45 (2008) 473–484.
[17] A. Kitagawa, K. Kitada, Y. Hagiwara, Experimental study on turbulent natural convection heat transfer in water with sub-millimeter-bubble injection, Exp. Fluids 49 (2010) 613–622.
[18] A. Kitagawa, Y. Murai, Natural convection heat transfer from a vertical heated plate in water with microbubble injection, Chem. Eng. Sci. 99 (2013) 215–224.
[19] A. Kitagawa, P. Denissenko, Y. Murai, Effect of wall surface wettability on collective behavior of hydrogen microbubbles rising along a wall, Exp. Ther. Fluid Sci. 80 (2017) 126–138.
[20] R.H.S. Winterton, Effect of Gas Bubbles on Liquid Metal Heat Transfer, Int. J. Heat Mass Transfer 17 (1974) 549–554.
[21] D.B.R. Kenning, Y.S. Kao, Convective heat transfer to water containing bubbles: enhancement not dependent on thermocapillarity, Int. J. Heat Mass Transfer 15 (1972) 1709–1717.
[22] J.Y. Kim, A.J. Ghajar, A general heat transfer correlation for nonboiling gas-liquid flow with different flow patterns in horizontal pipes, Int. J. Multiphase Flow 32 (2006) 447–465.
[23] R. Zimmerman, M. Gurevich, A. Mosyak, R. Rozenblit, G. Hetsroni, Heat transfer to air-water annular flow in a horizontal pipe, Int. J. Multiphase Flow 32 (2006) 1–19.
[24] S. Yanase, K. Matsuura, Recent Development of the Micro-bubble Science, Nagare 34 (2015) 355–362. (in Japanese)
[25] D. Qiu, V.K. Dhir, Experimental study of flow pattern and heat transfer associated with a bubble sliding on downward facing inclined surfaces, Exp. Ther. Fluid Sci. 26 (2002) 605–616.
[26] B.B. Bayazit, D.K. Hollingsworth, L.C. Witte, Heat transfer enhancement caused by sliding bubbles, J. Heat Transfer 125 (2003) 503–509.
[27] Y.M.C. Delaure, V.S.S. Chan, D.B. Murray, A simultaneous PIV and heat transfer study of bubble interaction with free convection flow, Exp. Ther. Fluid Sci. 27 (2003) 911–926.
[28] K.M. DeBisschop, M.J. Miksis, D.M. Eckmann, Bubble rising in an inclined channel, Phys. Fluids 14 (2002) 10.1063/1.1425842
[29] C. Brucker, Structure and dynamics of the wake of bubbles and its relevance for bubble interaction, Phys. Fluids 11 (1999) 1781–1796.
[30] A. Fujiwara, Y. Danmoto, K. Hishida, M. Maeda, Bubble deformation and flow structure measured by double shadow images and PIV/LIF, Exp. Fluids 36 (2004) 157–165.
[31] A. Kitagawa, Y. Hagiwara, T. Kouda, PTV investigation of phase interaction in dispersed liquid-liquid two-phase turbulent swirling flow, Exp. Fluids 42 (2007) 871–880.
[32] G.C. Vliet, Natural convection local heat transfer on constant-heat-flux inclined surfaces, Trans. ASME J. Heat Transfer 91 (1969) 511–516.
[33] J.R. Lloyd, E.M. Sparrow, E.R.G. Eckert, Laminar, transition and turbulent natural convection adjacent to inclined and vertical surfaces, Int. J. Heat Mass Transfer 15 (1972) 457–473.
[34] T. Fujii, H. Imura, Natural-convection heat transfer from a plate with arbitrary inclination, Int. J. Heat Mass Transfer 15 (1972) 755–767.
[35] H. Shaukatullah, B. Gebhart, An experimental investigation of natural convection flow on an inclined surface,

Int. J. Heat Mass Transfer 21 (1978) 1481–1490.
[36] K. Kitamura, J. Matsumoto, A. Mitsuishi, T. Misumi, Fluid flow and heat transfer of opposing mixed convection adjacent to downward-facing, inclined heated plates, Heat Transfer-Asian Research 38 (2009) 25–39.
[37] G.C. Vliet, C.K. Liu, An experimental study of turbulent natural convection boundary layers, Trans. ASME J. Heat Transfer 91 (1969) 517–531.
[38] A. Kitagawa, Y. Murai, Pulsatory rise of microbubble swarm along a vertical wall, Chem. Eng. Sci. 116 (2014) 694–703.
[39] S. Takagi, Y. Matsumoto, Surfactant effects on bubble motion and bubbly flows, Annu. Rev. Fluid Mech. 43 (2011) 615–636.
[40] C. Barbosa, D. Legendre, R. Zenit1, Conditions for the sliding-bouncing transition for the interaction of a bubble with an inclined wall, Phys. Rev. Fluids 1 (2016) 032201(R).
[41] H.K. Tsao, D.L Koch, Observations of high Reynolds number bubbles interacting with a rigid wall, Phys. Fluids 9 (1997) 45–56.
[42] A.W.G. de Vries, A. Biesheuvel, L.van Wijngaarden, Notes on the path and wake of a gas bubble rising in pure water, Int. J. Multiphase Flow 28 (2002) 1823–1835.
[43] Y. Hattori, T. Tsuji, Y. Nagano, N. Tanaka, Turbulence characteristics of natural-convection boundary layer in air along a vertical plate heated at high temperatures, Int. J. Heat Fluid Flow 27 (2006) 445–455.

Table 1

Experimental conditions used for temperature measurements.

Initial liquid temperature	T_L = 22 ˚C
Inclination angle of heated plate	ϕ = 0, 20, 40˚
Wall heat flux	q_W = 1480 W/m^2
Bubble flow rate	Q = 100 ml/min
Measurement position (T_W)	x = 70, 170, 270, 370, 470, 570, 670, 770 mm, z = −25, 0, 25 mm
Measurement position ($T_{L\infty}$)	x = 370 mm, y = 175 mm, z = 0 mm
Measurement position (T_L)	x = 170 mm, z =0 mm

Table 2

Experimental conditions used for velocity measurements.

Initial liquid temperature	T_L = 22 ˚C
Inclination angle of heated plate	ϕ = 0, 20, 40˚
Wall heat flux	q_W = 1480 W/m^2
Bubble flow rate	Q = 100 ml/min
Measurement position	x = 170 mm, z =−10 mm

Table 3

Thickness of effective thermal boundary layer δ_{TE} and thickness of actual thermal boundary layer δ_T for cases with and without bubble injection at each wall inclination angle (TPF: two-phase flow, SPF: single-phase flow).

ϕ (˚)	δ_{TE} [SPF] (mm)	δ_{TE} [TPF] (mm)	δ_T [SPF] (mm)	δ_T [TPF] (mm)
0	2.0	0.7	4.6	9.4
20	2.0	0.5	4.9	14.7
40	2.1	0.4	5.3	19.0

Table 4

Ratio of actual thermal boundary layer thickness δ_T to velocity boundary layer thickness δ_V for cases with and without bubble injection at each wall inclination angle (TPF: two-phase flow, SPF: single-phase flow).

ϕ	δ_T/δ_V [SPF]	δ_T/δ_V [TPF]
(°)	(–)	(–)
0	0.31	0.31
20	0.34	0.55
40	0.36	0.69

Table 5

Wall-parallel velocity of liquid phase averaged over effective thermal boundary layer thickness $u_{L\delta}$ and eddy diffusivity in boundary layer K_{eddy} at each wall inclination angle (TPF: two-phase flow, SPF: single-phase flow)

ϕ	$u_{L\delta}$ [SPF]	$u_{L\delta}$ [TPF]	K_{eddy}	ν	α
(°)	(mm/s)	(mm/s)	$\times 10^{-6}$ (m^2/s)	$\times 10^{-6}$ (m^2/s)	$\times 10^{-6}$ (m^2/s)
0	7.3	35.8	8.3	0.96	0.14
20	7.4	51.1	9.0	0.96	0.14
40	6.7	44.1	10.7	0.96	0.14

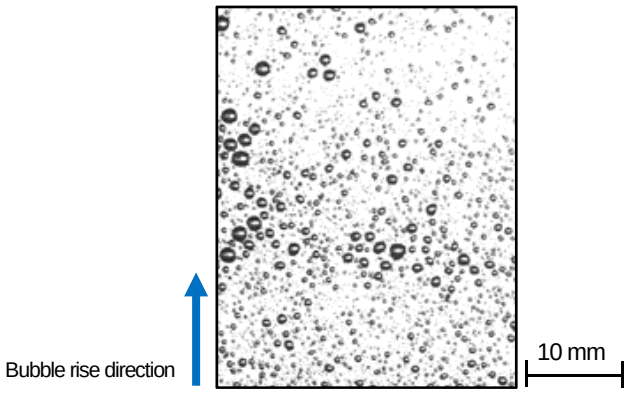

Fig. 1. Image of bubbles attached to a vertical wall from stream of rising microbubbles. The Sauter mean diameter of injected bubbles is initially 110 μm.

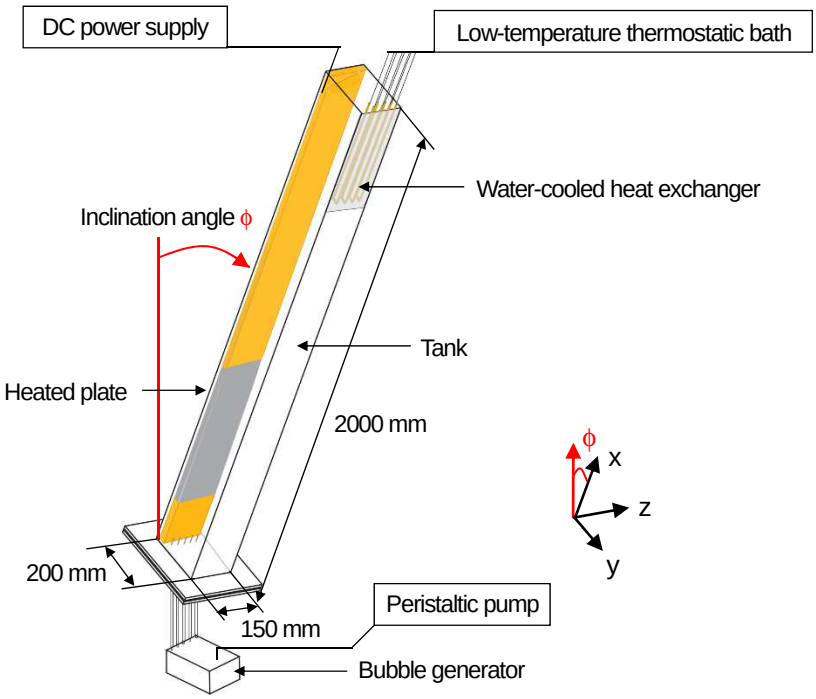

Fig. 2. Schematic of the experimental apparatus.

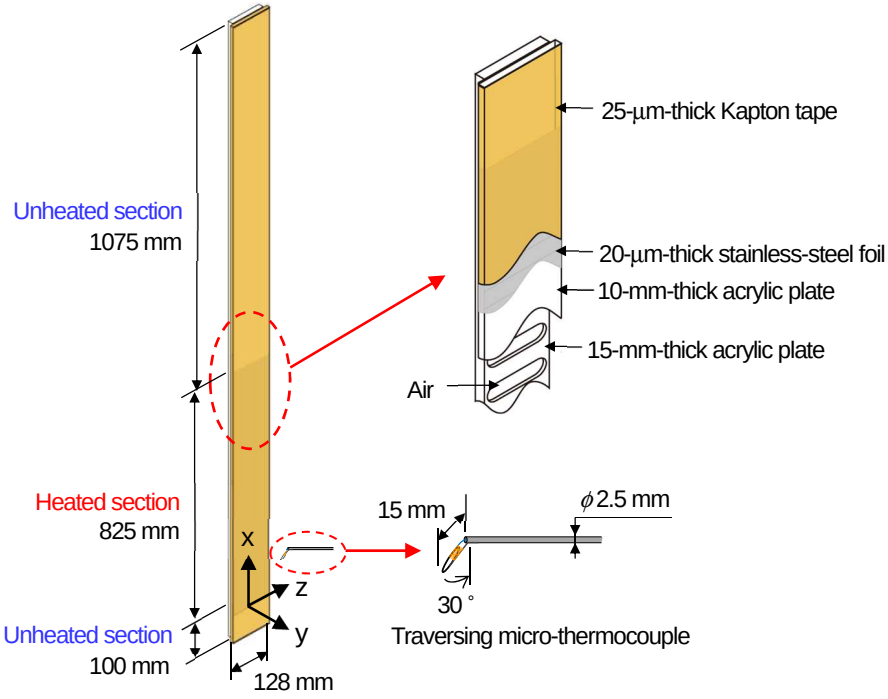

Fig. 3. Schematic of the heated plate.

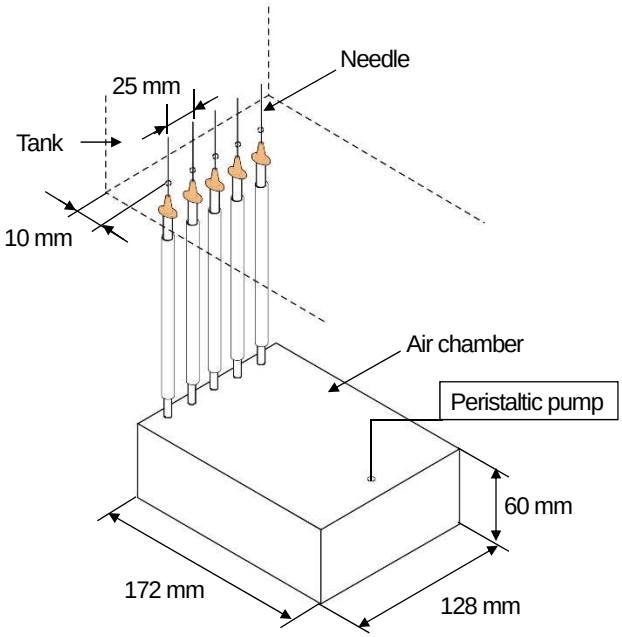

Fig. 4. Schematic of the bubble generator.

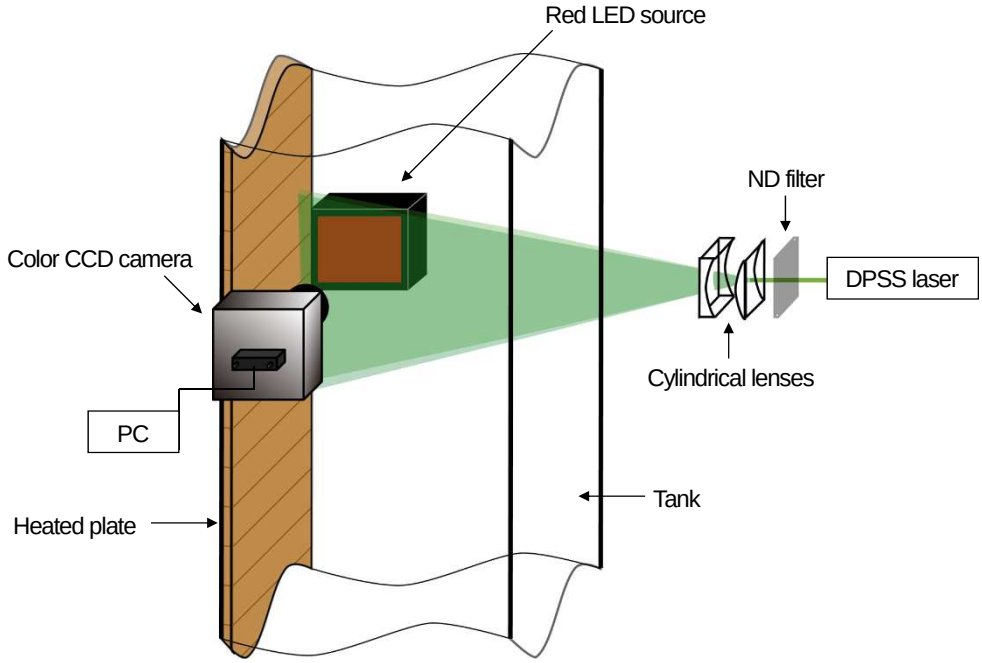

Fig. 5. Schematic of the two-phase velocity measurement system.

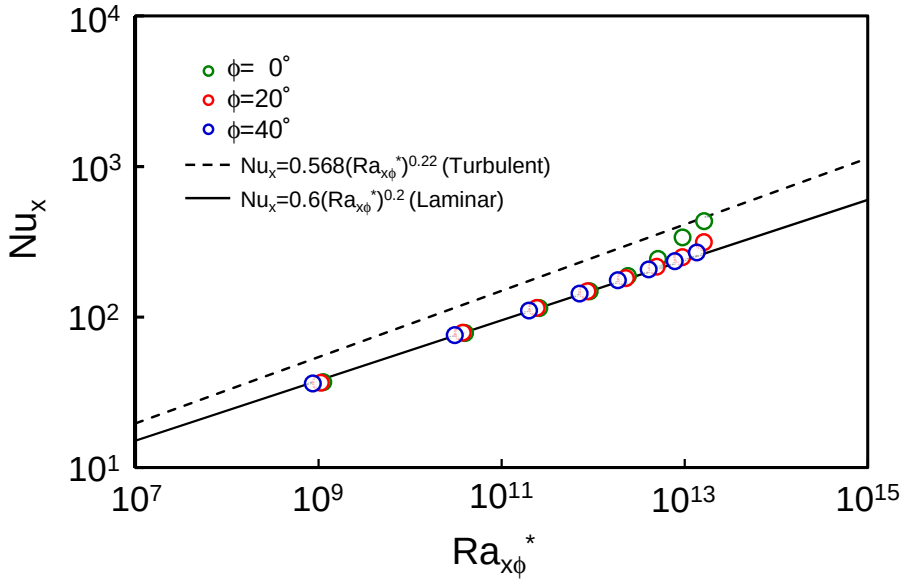

Fig. 6. Relationship between modified Rayleigh number $Ra_{x\phi}^*$ and local Nusselt number Nu_x without bubble injection. The circles are experimental data, and the solid and dashed lines are empirical equations.

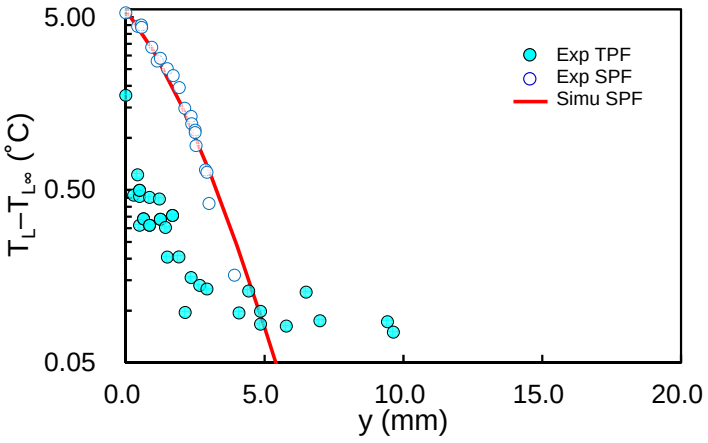

(a) ϕ=0°

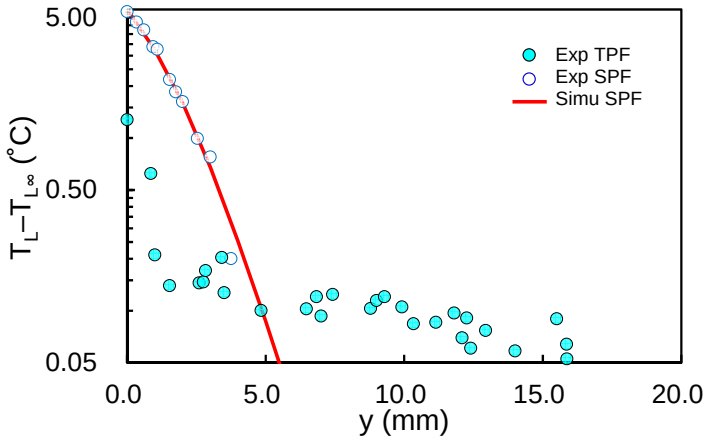

(b) ϕ=20°

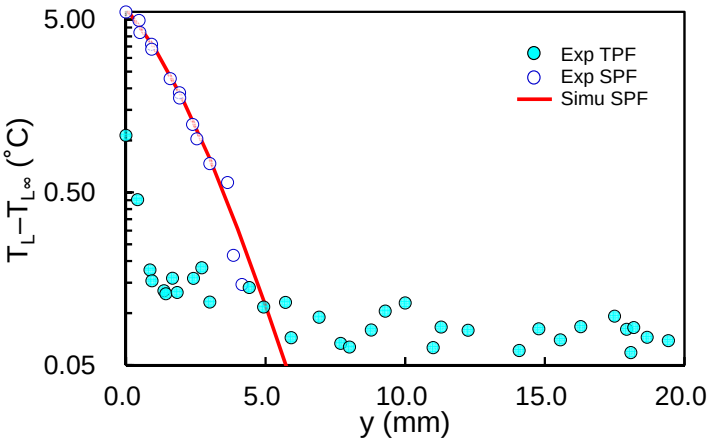

(c) ϕ=40°

Fig. 7. Distributions of liquid temperature difference $T_L - T_{L\infty}$ with and without bubble injection (TPF: two-phase flow, SPF: single-phase flow). The simulation results for SPF were obtained by our research group.

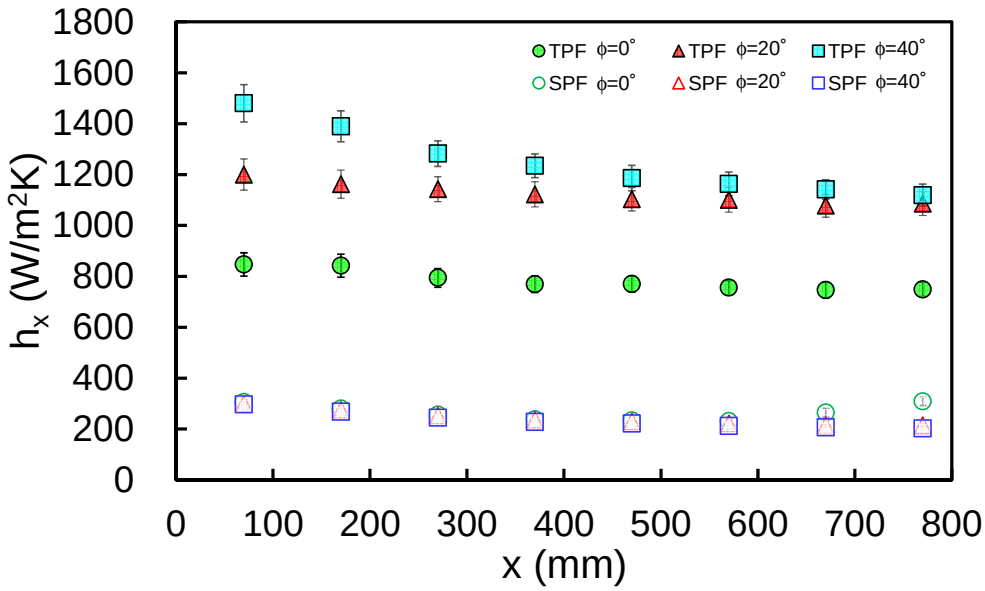

Fig. 8. Relationship between measurement position *x* and heat transfer coefficient h_x with and without bubble injection (TPF: two-phase flow, SPF: single-phase flow). The error bars indicate the standard deviation of the data.

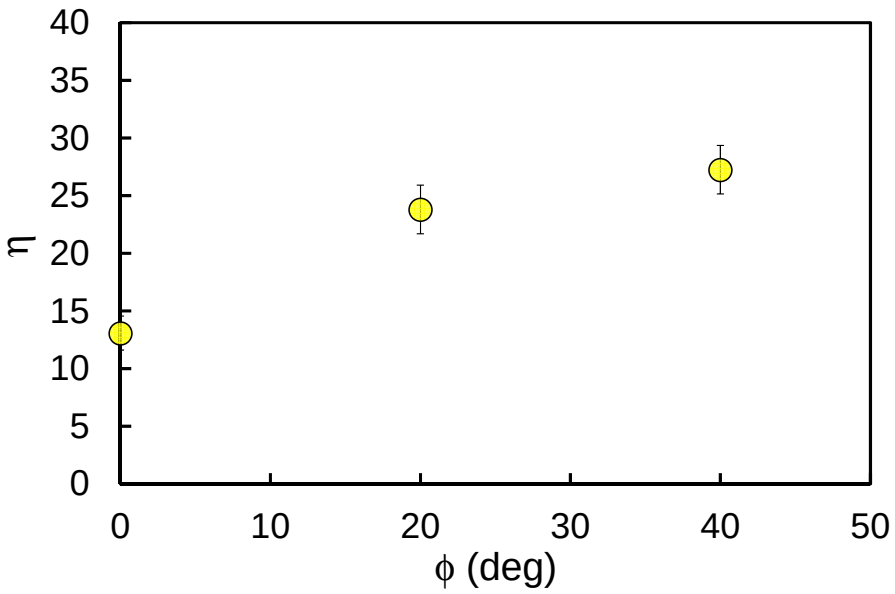

Fig. 9. Relationship between inclination angle of heated plate ϕ and efficiency of bubble injection η. The error bars indicate the standard deviation of the data.

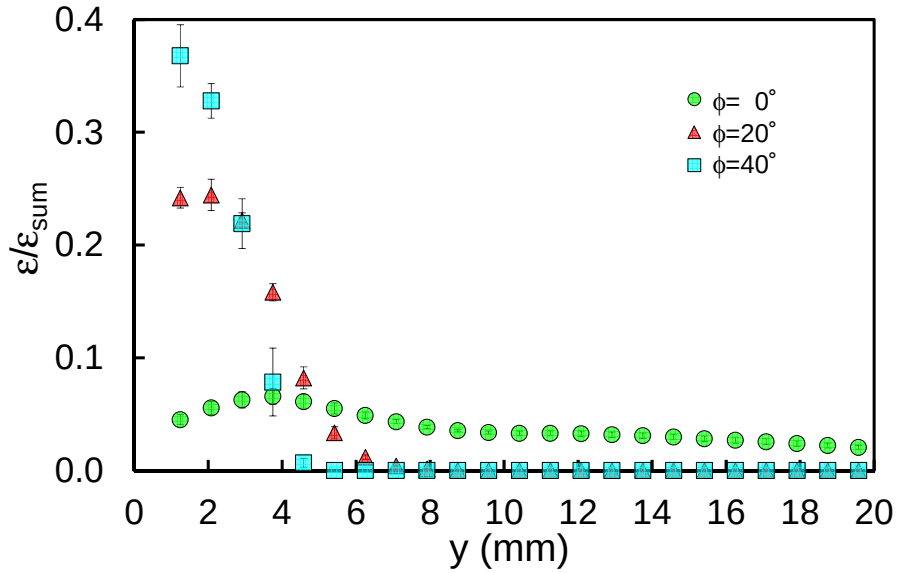

Fig. 10. Profiles of bubble concentration in wall-normal direction ε (ε_{sum}: sum of ε). The error bars indicate the standard deviation of the data.

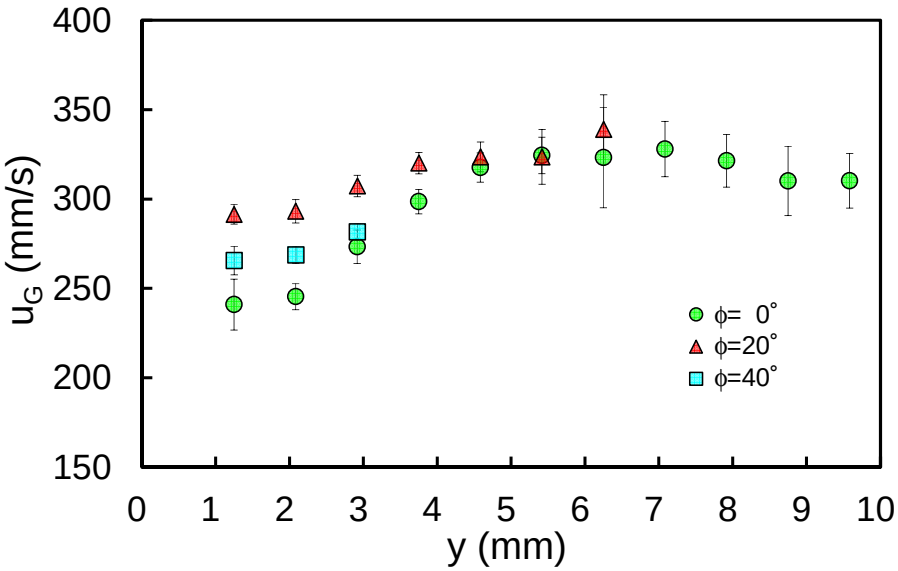

Fig. 11. Profiles of wall-parallel mean velocity of bubbles u_G. The error bars indicate the standard deviation of the data.

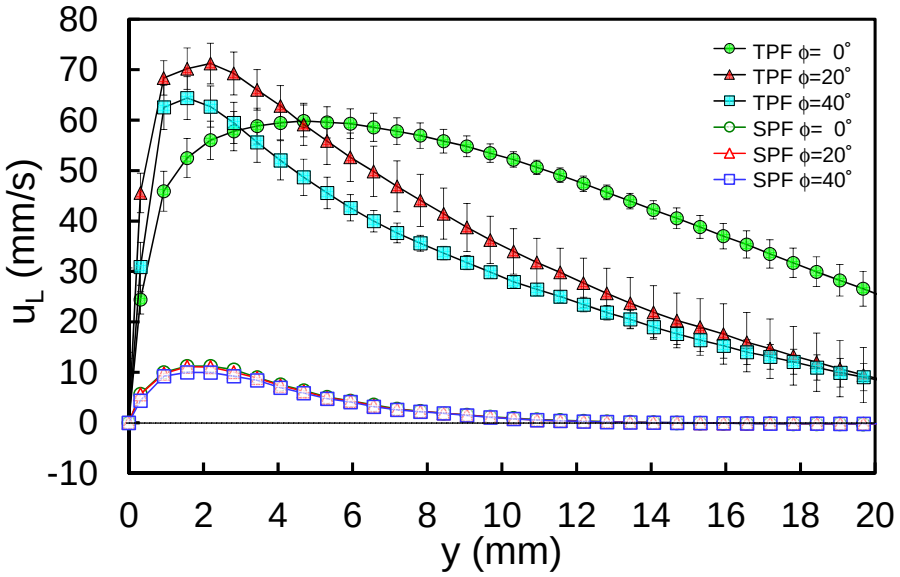

Fig. 12. Profiles of wall-parallel mean velocity of liquid phase u_L with and without bubble injection (TPF: two-phase flow, SPF: single-phase flow). The error bars indicate the standard deviation of the data.

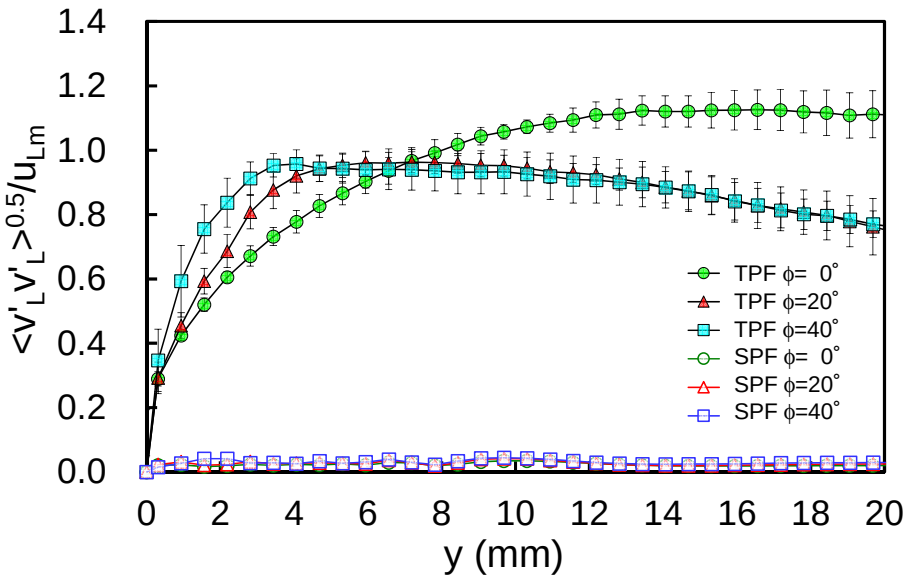

Fig. 13. Profiles of RMS of wall-normal fluctuation velocity of liquid phase $\langle v'_L v'_L \rangle^{0.5}$ with and without bubble injection (TPF: two-phase flow, SPF: single-phase flow, u_{Lm}: maximum value of wall-parallel mean velocity of liquid phase without bubble injection). The error bars indicate the standard deviation of the data.

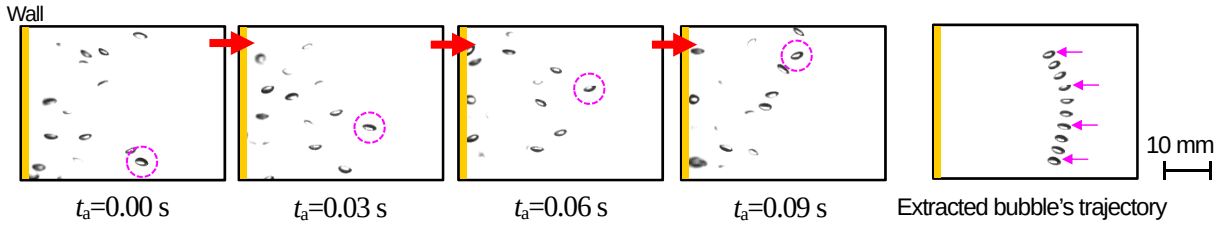

(a) ϕ=0˚

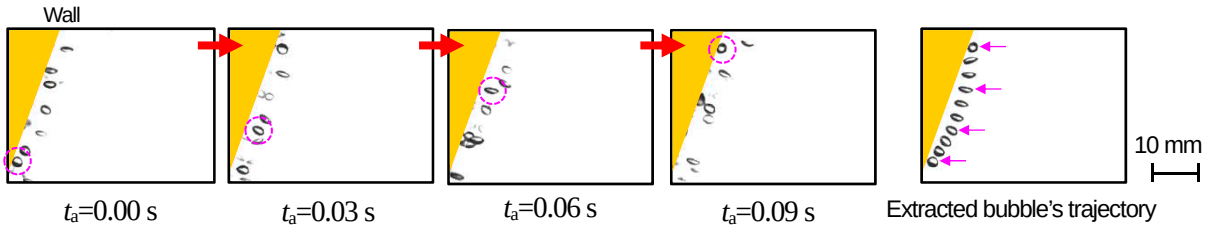

(b) ϕ=20˚

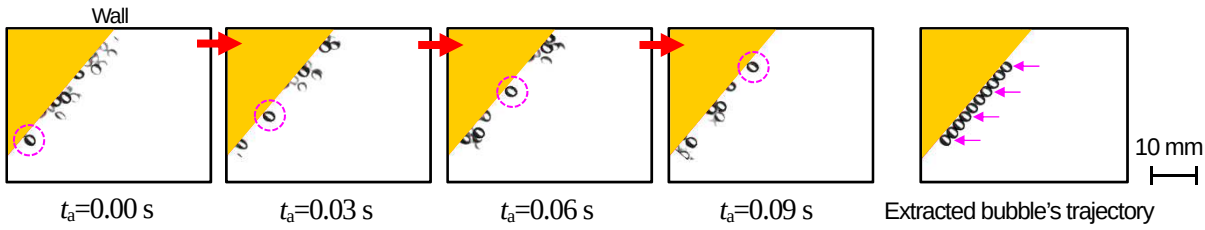

(c) ϕ=40˚

Fig. 14. Typical time-series images of bubbles near heated wall.

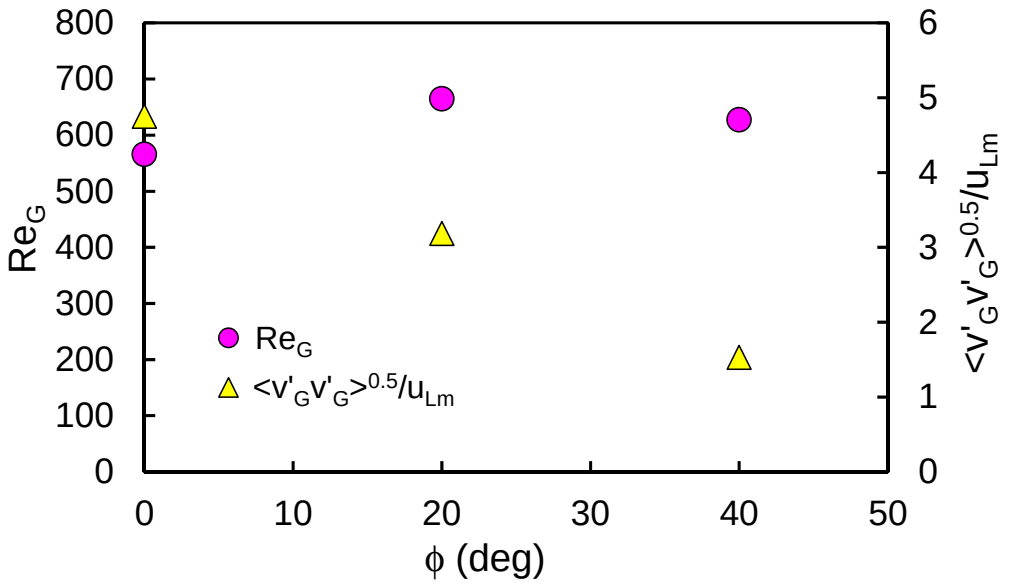

Fig. 15. Bubble Reynolds number Re_G and RMS of wall-normal fluctuation velocity of bubbles $\langle v'_G v'_G \rangle^{0.5}$ as a function of inclination angle of heated plate ϕ (u_{Lm}: maximum value of wall-parallel mean velocity of liquid phase without bubble injection).

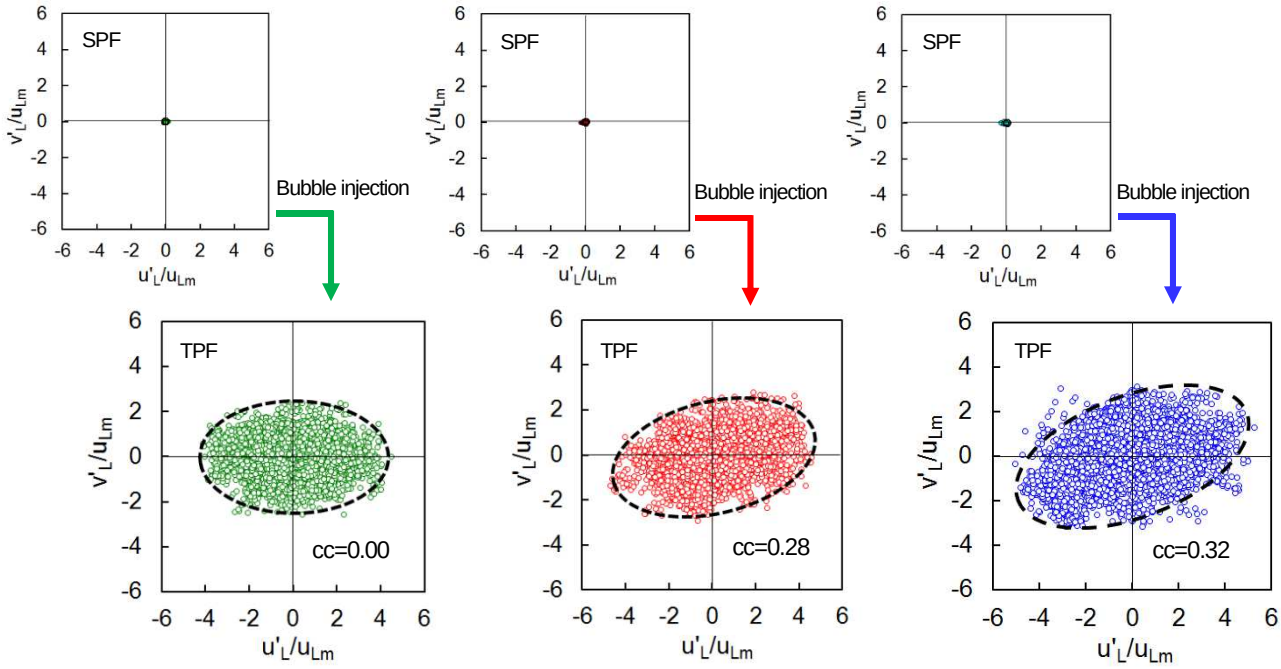

(a) ϕ=0˚ (b) ϕ=20˚ (c) ϕ=40˚

Fig. 16. Scatter plots of wall-parallel liquid fluctuation velocity u'_L and wall-normal liquid fluctuation velocity v'_L with and without bubble injection (TPF: two-phase flow, SPF: single-phase flow, u_{Lm}: maximum value of wall-parallel mean velocity of liquid phase without bubble injection, *cc*: correlation coefficient between u'_L and v'_L).

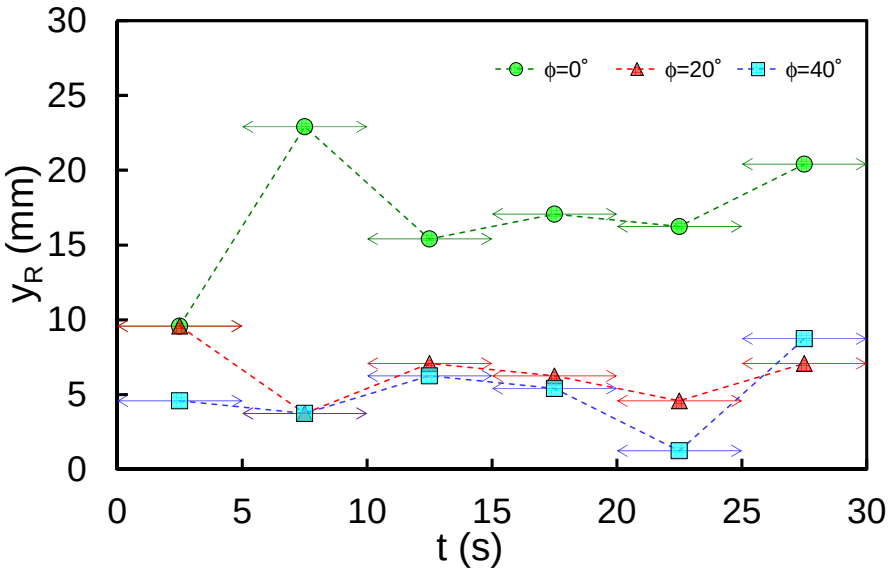

Fig. 17. Time evolution of distance between location of peak in Reynolds shear stress profile and heated wall y_R with bubble injection.

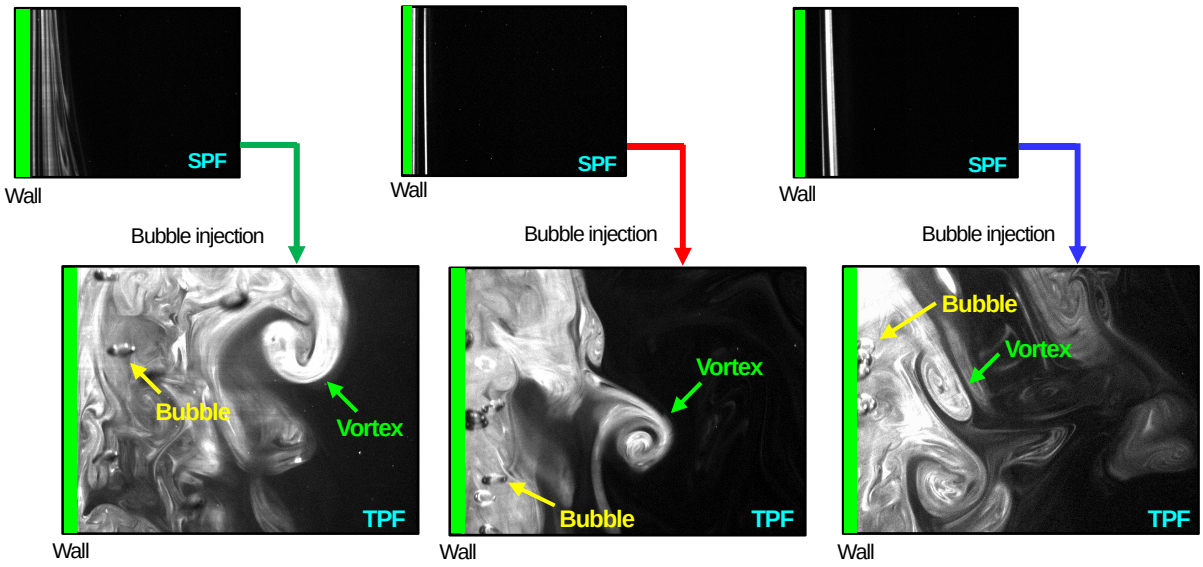

(a) ϕ=0˚ (b) ϕ=20˚ (c) ϕ=40˚

Fig. 18. Flow visualization using fluorescent dye.

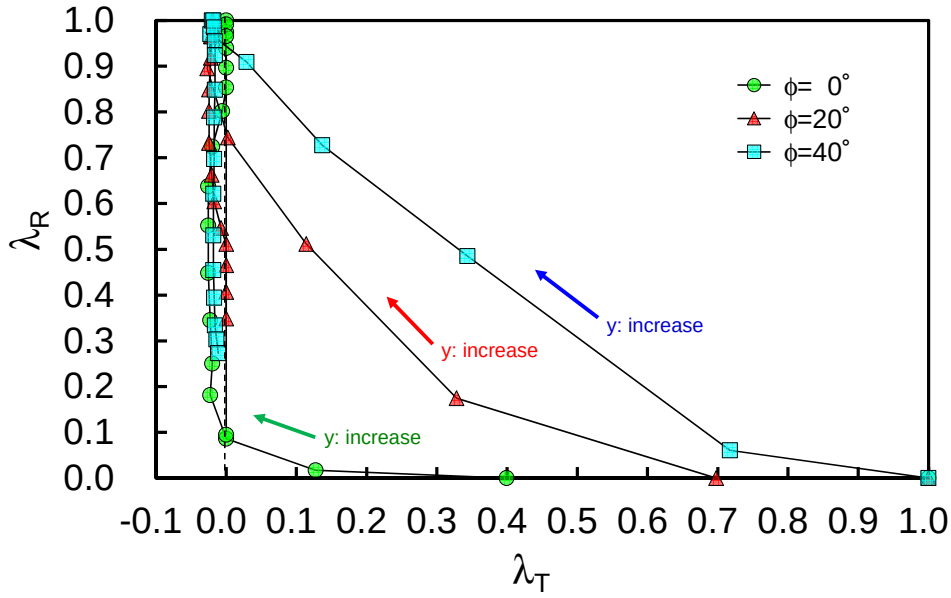

Fig. 19. Relationship between normalized liquid temperature reduction by bubble injection λ_T and normalized Reynolds shear stress λ_R. λ_T and λ_R are defined as $\lambda_T=(T_{L\_SPF}-T_{L\_TPF})/|T_{W\_SPF}-T_{W\_TPF}|$ and $\lambda_R=\langle u'_L v'_L\rangle/\langle u'_L v'_L\rangle_m$, respectively.

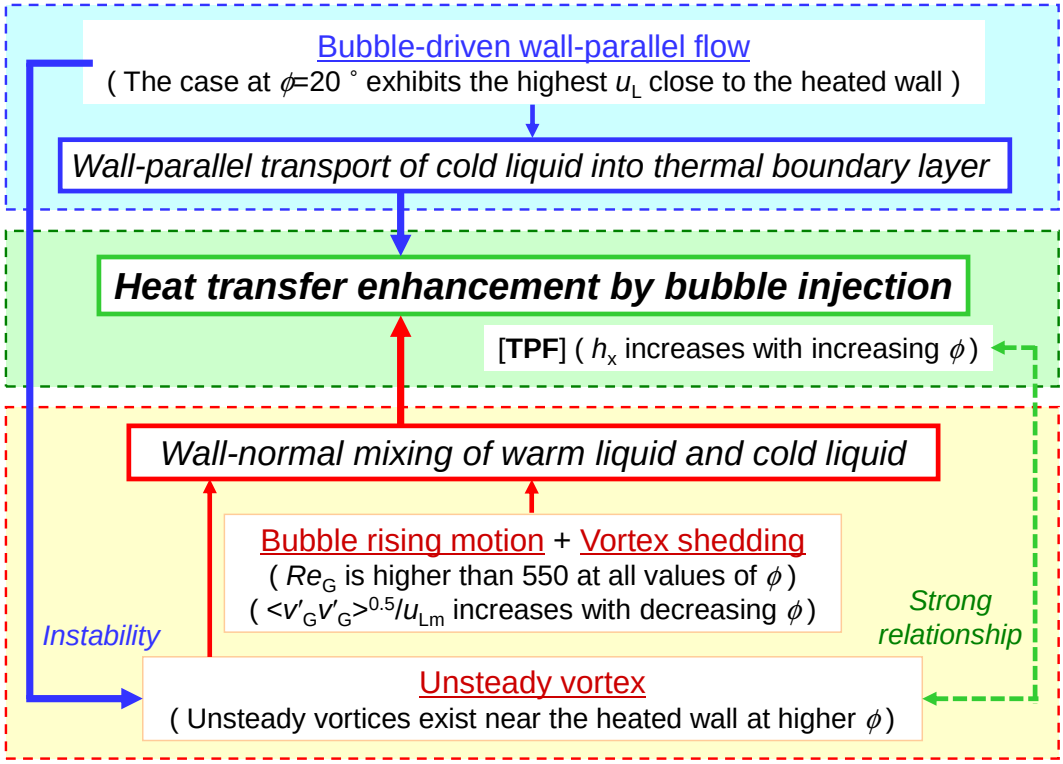

Fig. 20. Summary of mechanism of heat transfer enhancement by near-wall injection of millimeter-sized bubbles (TPF: two-phase flow, u_L: wall-parallel velocity of liquid phase, h_x: heat transfer coefficient, Re_G: bubble Reynolds number, $<v'_G v'_G>^{0.5}$: RMS of wall-normal fluctuation velocity of bubbles, u_{Lm}: maximum value of wall-parallel mean velocity of liquid phase without bubble injection).

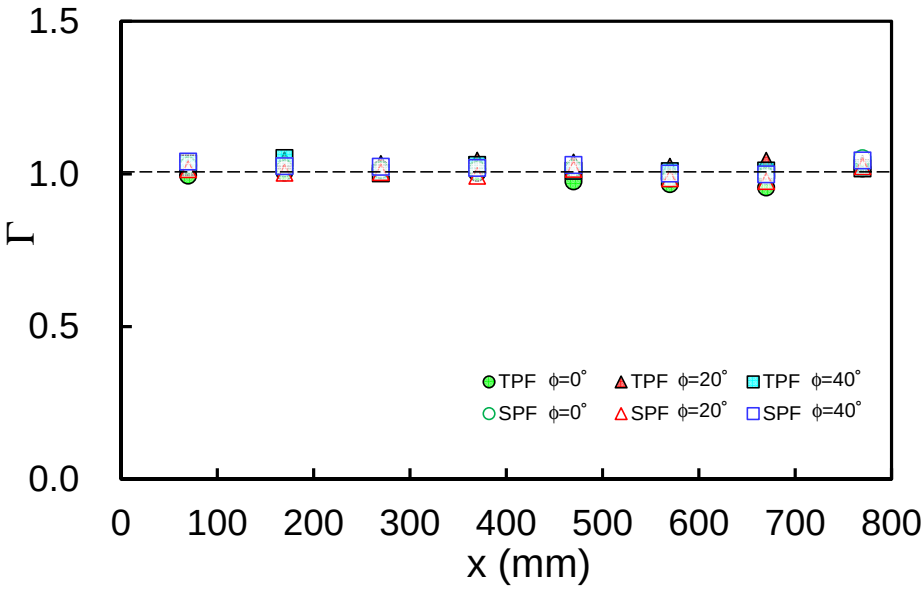

Fig. A.1. Comparison of heat transfer coefficients with and without a traversing micro-thermocouple (TPF: two-phase flow, SPF: single-phase flow).

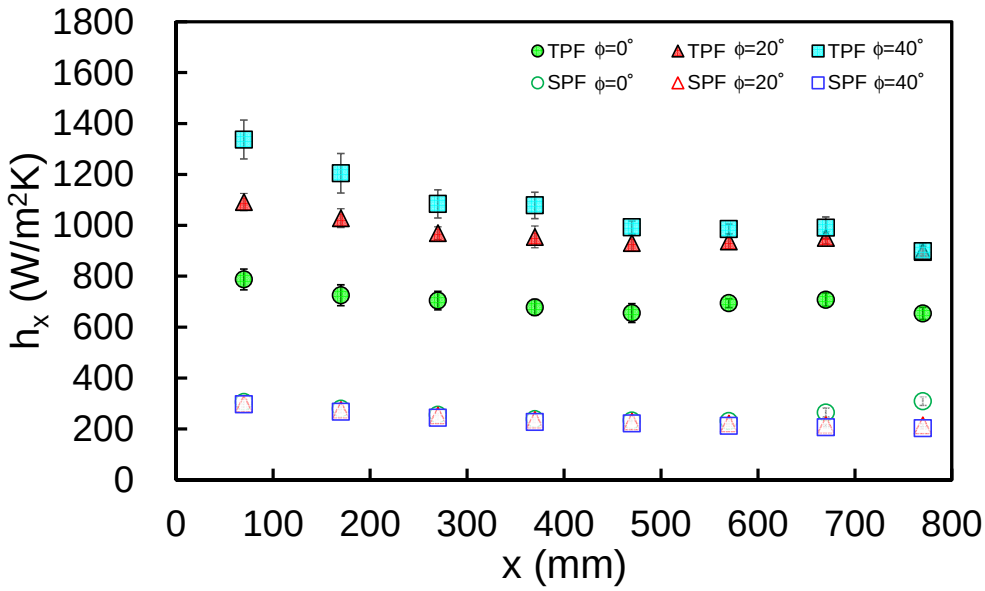

Fig. B.1. Relationship between measurement position *x* and heat transfer coefficient h_x at bubble flow rate of 50 ml/min (TPF: two-phase flow, SPF: single-phase flow). The error bars indicate the standard deviation of the data.